Appl. Phys. B 67, 449–458 (1998)

Applied Physics B
Lasers
and Optics

Photoacoustic multicomponent gas analysis using a Levenberg–Marquardt fitting algorithm

M.A. Moeckli*, C. Hilbes, M.W. Sigrist

ETH Zürich, Institute of Quantum Electronics, CH-8093 Zürich, Switzerland
(Fax: +41-1/633-1077, E-mail: sigrist@iqe.phys.ethz.ch)

Received: 23 March 1998/Revised version: 18 June 1998

Abstract. A mobile CO_2 laser photoacoustic spectrometer has been developed for the in-situ monitoring of atmospheric trace gases in different environments. Numerous air pollutants, such as ammonia, ethene, ozone and alcohols, can be monitored with a time resolution of a few minutes. A new fitting algorithm based on the numerical method of Levenberg–Marquardt is discussed and applied to the derivation of individual gas concentrations from measured photoacoustic signal amplitudes and phases at selected CO_2 laser wavelengths. The algorithm has been tested with artificially generated multicomponent gas mixtures exhibiting gas concentrations in the ppb to ppm range. Furthermore, its potential is demonstrated with the analysis of an air sample from a fruit storage chamber and with ambient air measurements during a field study in a rural environment.

PACS: 82.80.Kq; 02.60.+y; 89.60.+x

In photoacoustic (PA) spectroscopy the radiation absorbed by gas molecules in an absorption cell is detected purely acoustically. Molecular energy transfer processes convert energy stored in excited vibrational modes of the molecules into acoustic waves that can be detected with microphones. The CO_2 laser is a suitable radiation source, since it provides powerful radiation in the wavelength range between 9 and 11 μm in which numerous molecules exhibit characteristic strong absorption bands. By modulating the exciting laser beam at an acoustic resonance frequency of the absorption cell a high sensitivity can be achieved that allows the detection of absorption coefficients as low as $10^{-8}\,\mathrm{cm}^{-1}$ [1]. This technique thus allows the monitoring of numerous organic and inorganic compounds at ppb concentrations. One problem associated with resonant PA spectroscopy at CO_2 laser wavelengths concerns the amplitude of the detected acoustic signal and its phase with respect to the modulated exciting radiation, which are both influenced by the amount of water vapor and CO_2 present in the gas sample. This is caused by resonant energy transfer processes between vibrational energy levels of excited molecules, the most important being the energy transfer between the first mode of the asymmetric stretch vibration of CO_2 and a nearby energy level of nitrogen, the prevalent compound in ambient air.

These effects were first described by Wood et al. [2] and are referred to in literature as kinetic cooling effects, since they result in an initial cooling of the absorbing gas sample. In previous analyses of multicomponent air samples containing water vapor and CO_2 we have used the in-phase part of the PA signals in a weighted linear least squares fit of the measured spectra [3]. Several difficulties are, however, imposed by this approach: since only the in-phase part of the signal is used for the analysis, half of the information entailed in the measurement is lost in the calculations. In practice, an additional phase offset resulting from the experiment can be superposed to the theoretical photoacoustic phase. Since this parameter can vary with the measurement conditions it is difficult to determine in advance. This problem has been accounted for by restricting the analysis to phase lags of π in the case of dominant CO_2 absorption and of 0° in other situations and by determining the phase offset manually [4]. Particularly at larger CO_2 concentrations, which typically occur in polluted ambient air, the photoacoustic phase can, however, assume values between 0° and π. This is revealed by the examples of multicomponent analyses presented below.

Rooth et al. [5] have added ammonia as a further component to the idealized atmosphere in Wood's model and calculated the resonant PA signal amplitude and phase at selected CO_2 laser wavelengths. They considered an atmosphere that, besides oxygen and nitrogen, contained only CO_2, water vapor and ammonia, and they derived ambient ammonia concentrations during a field study in the Netherlands. We have extended this model and developed a fitting algorithm with the numerical method of Levenberg–Marquardt that derives unknown gas concentrations not only for ammonia but simultaneously for a number of trace components from the meas-

* *Present address*: ARITRON INSTRUMENTE AG, CH-8127 Forch, Switzerland

ured resonant PA amplitude and phase spectra at $^{12}C^{16}O_2$ laser wavelengths.

1 Theoretical model

We briefly review the model used by Rooth et al. [5] that results in equations for the PA signal amplitude and phase at a given CO_2 laser frequency. Therefore we identify the main components of our model atmosphere by the indices $H \equiv H_2O$, $C \equiv CO_2$, $N \equiv N_2$ and $O \equiv O_2$. As an important and substantial extension we include additional trace components in the analysis. These are all denoted by the index i and we use the Einstein sum convention for shorter notation, i.e. $\alpha_i c_i \equiv \sum_i \alpha_i c_i$.

In analogy to the method of Rooth et al. [5] we assume that no further resonant effects occur between energy levels of the additional components than those discussed by Wood et al. [2]. This approach is well justified from our experience. The dependence of the enthalpy H of a gas sample in the absorption cell is determined by the absorption of laser radiation by the individual components, by the energy transfer to and from vibrationally excited nitrogen and by the heat loss of the gas sample at the walls of the absorption cell. For a gas sample of unit volume these processes obey

$$\frac{\mathrm{d}H}{\mathrm{d}t} = (\alpha_\mathrm{H} c_\mathrm{H} + \alpha_\mathrm{C} c_\mathrm{C} + \alpha_i c_i) I(t) - \frac{\mathrm{d}E_\mathrm{N}}{\mathrm{d}t} - \left(\frac{H(t) - H(0)}{\tau_\mathrm{s}}\right) . \tag{1}$$

Here the α_x denote the wavelength-dependent absorption coefficient per unit length and normalized to concentration 1. The c_x denote the dimensionless absolute concentration of the compound x and $I(t)$ stands for the intensity of the irradiating radiation, i.e. the number of photons per unit area and per time multiplied by their energy, E_N denotes the energy stored in vibrationally excited nitrogen molecules per unit volume and τ_s the characteristic time for heat losses of the PA cell [6]. The small energy gap, known as Fermi resonance [7], between the $CO_2(100)$ and the $CO_2(02^10)$ vibrational states of approximately $7\,\mathrm{cm}^{-1}$ is small compared to the thermal energy at room temperature of $kT \approx 200\,\mathrm{cm}^{-1}$. Thus thermal equilibrium of the populations of these states can be assumed for further calculations. For similar reasons thermal equilibrium is assumed among the vibrationally excited nitrogen molecules (N_2^*) and the $CO_2(001)$ mode and among the O_2 mode and the ν_2 mode of H_2O. Finally the ν_2 vibration modes of CO_2 and H_2O are assumed to be in thermal equilibrium with the translational states of the molecules.

The above assumptions are summarized as

$$E_{\mathrm{CO}_2^*(\nu_3)} \approx E_{\mathrm{N}_2^*} , \tag{2}$$

$$E_{\mathrm{CO}_2^*(\nu_1)} \approx E_{\mathrm{CO}_2^*(2\nu_2)} \approx E_{\mathrm{H_2O^*}} \approx E_{\mathrm{O}_2^*} . \tag{3}$$

According to Wood et al. [2] the rate of change of the vibrational energy of N_2^* at ambient atmospheric conditions is given by

$$\frac{\mathrm{d}E_\mathrm{N}}{\mathrm{d}t} = \frac{E_\mathrm{N}(0) - E_\mathrm{N}(t)}{\tau_\mathrm{N}} + \beta\alpha_\mathrm{C} c_\mathrm{C} I(t) , \tag{4}$$

where the coefficient β is defined as the ratio of the energy of the excited state to the energy of the exciting photon, i.e. $\beta = h\nu_{001}/h\nu_l$, with $\nu_l = \nu_{001} - \nu_{100}$ for the 10-μm branch and $\nu_l = \nu_{001} - 2\nu_{010}$ for the 9-μm branch.

For the relaxation time of N_2^*, Wood et al. [2] assumed

$$\frac{1}{\tau_\mathrm{N}} = \left(\frac{c_\mathrm{H}}{\tau_\mathrm{CH}} + \frac{c_\mathrm{N}}{\tau_\mathrm{CN}} + \frac{c_\mathrm{O}}{\tau_\mathrm{CO}}\right)\frac{c_\mathrm{C}}{c_\mathrm{N}} + \frac{c_\mathrm{H}}{\tau_\mathrm{NH}} + \frac{c_\mathrm{O}}{\tau_\mathrm{NO}} , \tag{5}$$

where τ_{ij} denotes the relaxation time for the vibrational–translational energy exchange between the molecules i and j. Data relevant for the calculation of the PA signal in our idealized atmosphere are presented in Table 1. In resonant photoacoustic spectroscopy the acoustic modes of the absorption cell are excited by intensity-modulated laser radiation of the form

$$I(t) = I_0\left(1 + \mathrm{e}^{\mathrm{i}\omega t}\right) . \tag{6}$$

With the additional restriction $t \gg \tau_\mathrm{N}$, (4) can be modified to give

$$\frac{\mathrm{d}E_\mathrm{N}(t)}{\mathrm{d}t} = \beta\alpha_\mathrm{C} c_\mathrm{C} \frac{\mathrm{i}\omega\tau_\mathrm{N} I_0 \mathrm{e}^{\mathrm{i}\omega t}}{1 + \mathrm{i}\omega\tau_\mathrm{N}} . \tag{7}$$

Introducing this term into (1) and solving for $H(t)$, one finds for the time development of the system's enthalpy the real part of

$$\begin{aligned} H(t) &= H(0) + I_0\tau_\mathrm{s}\left[\alpha_\mathrm{H} c_\mathrm{H} + \alpha_\mathrm{C} c_\mathrm{C} + \alpha_i c_i\right]\left(1 - \mathrm{e}^{-t/\tau_\mathrm{s}}\right) \\ &\quad + \frac{I_0\tau_\mathrm{s}}{1 + \mathrm{i}\omega\tau_\mathrm{s}}\left[\alpha_\mathrm{H} c_\mathrm{H} + \alpha_\mathrm{C} c_\mathrm{C} + \alpha_i c_i \right. \\ &\quad \left. - \alpha_\mathrm{C} c_\mathrm{C} \frac{\beta\mathrm{i}\omega\tau_\mathrm{N}}{1 + \mathrm{i}\omega\tau_\mathrm{N}}\right]\left(\mathrm{e}^{\mathrm{i}\omega t} - \mathrm{e}^{-t/\tau_\mathrm{s}}\right) . \end{aligned} \tag{8}$$

The induced pressure change in the gas sample is proportional to the change of its enthalpy, the relevant part being

$$p(t) = A\frac{I_0\tau_\mathrm{s}}{1 + \mathrm{i}\omega\tau_\mathrm{s}}\left[\alpha_\mathrm{H} c_\mathrm{H} + \alpha_i c_i + \alpha_\mathrm{C} c_\mathrm{C}\left(1 - \frac{\beta\mathrm{i}\omega\tau_\mathrm{N}}{1 + \mathrm{i}\omega\tau_\mathrm{N}}\right)\right]\mathrm{e}^{\mathrm{i}\omega t} . \tag{9}$$

In polar coordinates we use the same notation as in [5]:

$$p(t) = R\mathrm{e}^{\mathrm{i}\theta}\mathrm{e}^{\mathrm{i}\omega t} , \tag{10}$$

with

$$R = A\sqrt{x^2 + y^2} \tag{11}$$

Table 1. Relaxation times for vibrational–translational energy exchange between the molecules i and j, calculated from data presented by Rooth et al. [5] and extrapolated to ambient atmospheric pressure of 950 hPa

Molecules i, j	τ_{ij}^{-1} /$\mathrm{Pa}^{-1}\mathrm{s}^{-1}$	τ_{ij} /s at $p = 950\,\mathrm{hPa}$
CO_2, N_2	0.902	11.67×10^{-6}
CO_2, O_2	0.940	11.20×10^{-6}
CO_2, H_2O	245.9	42.92×10^{-9}
N_2, H_2O	1.283	8.2×10^{-6}
N_2, O_2	0.000306	34.36×10^{-3}

and

$$\theta = \arctan\left(\frac{y}{x}\right) + \theta_0 \,. \tag{12}$$

The cartesian components are

$$p_x = \frac{I_0\tau_s}{1+(\omega\tau_s)^2}\omega\tau_s\Bigg[\frac{\alpha_i c_i + \alpha_H c_H + \alpha_C c_C}{\omega\tau_s} - \beta\alpha_C c_C \frac{\omega\tau_N}{1+(\omega\tau_N)^2}\left(\frac{\omega\tau_N}{\omega\tau_s}+1\right)\Bigg] \tag{13}$$

and

$$p_y = \frac{I_0\tau_s}{1+(\omega\tau_s)^2}\omega\tau_s\Bigg[-(\alpha_i c_i + \alpha_H c_H + \alpha_C c_C) + \beta\alpha_C c_C \frac{\omega\tau_N}{1+(\omega\tau_N)^2}\left(\frac{1}{\omega\tau_s}+\omega\tau_N\right)\Bigg] . \tag{14}$$

The characteristic time τ_s for heat losses of the gas sample is given by [6]

$$\frac{1}{\tau_s} = \frac{1}{\tau_T} + \frac{1}{\tau_L} \,, \tag{15}$$

where τ_T denotes the thermal relaxation time of the gas at the cell walls and τ_L is the characteristic time for gas exchange from the cell to adjacent volumina. In practice τ_s is of the order of 0.1 s to 1 s. For sufficiently high chopper frequencies it can therefore be assumed that $\omega\tau_s \gg 1$. This permits the following simplifications

$$\frac{1}{\omega\tau_s} \approx 0 \tag{16}$$

and

$$1+(\omega\tau_s)^2 \approx (\omega\tau_s)^2 \,. \tag{17}$$

Introduction of these terms into (13) and (14) finally yields the expressions for the measured resonant photoacoustic amplitude R and phase θ:

$$R = A\frac{I_0}{\omega}\left[\frac{(\alpha_i c_i + \alpha_H c_H + \alpha_C c_C)^2}{1+(\omega\tau_N)^2} + \frac{(\omega\tau_N)^2\left[\alpha_i c_i + \alpha_H c_H + (1-\beta)\alpha_C c_C\right]^2}{1+(\omega\tau_N)^2}\right]^{1/2} \tag{18}$$

$$\theta = \arctan\left(\frac{\alpha_i c_i + \alpha_H c_H + \alpha_C c_C}{\beta\alpha_C c_C}\left[\frac{1+(\omega\tau_N)^2}{\omega\tau_N}\right] - \omega\tau_N\right) + \theta_0 \,. \tag{19}$$

The proportionality factor A in (18) corresponds to the cell constant of the photoacoustic cell that is determined by calibration measurements. It depends on several parameters such as the geometry of the photoacoustic cell, its quality factor, the shape of the exciting laser beam and the pressure of the gas sample. Figure 1 illustrates the variations of the photoacoustic amplitude and phase at the main ethene absorption line 10P(14) in a gas sample containing 100 ppb ethene and variable CO_2 and water vapor concentrations. At constant absolute humidity and with increasing CO_2 concentration the signal amplitude decreases due to the kinetic cooling effect [2], passes a minimum at CO_2 concentrations between 1000 and 2000 ppm and finally increases when CO_2 absorption becomes dominant. Close to the minimum of the signal amplitude the signal phase rapidly changes and increases by 180°. The phase depicted in Fig. 1 has been inverted for comparison with the ethene, CO_2 and water vapor measurement discussed further below. The inverse phase in the experiment compared to the data calcutated with (20) is caused by the detection electronics.

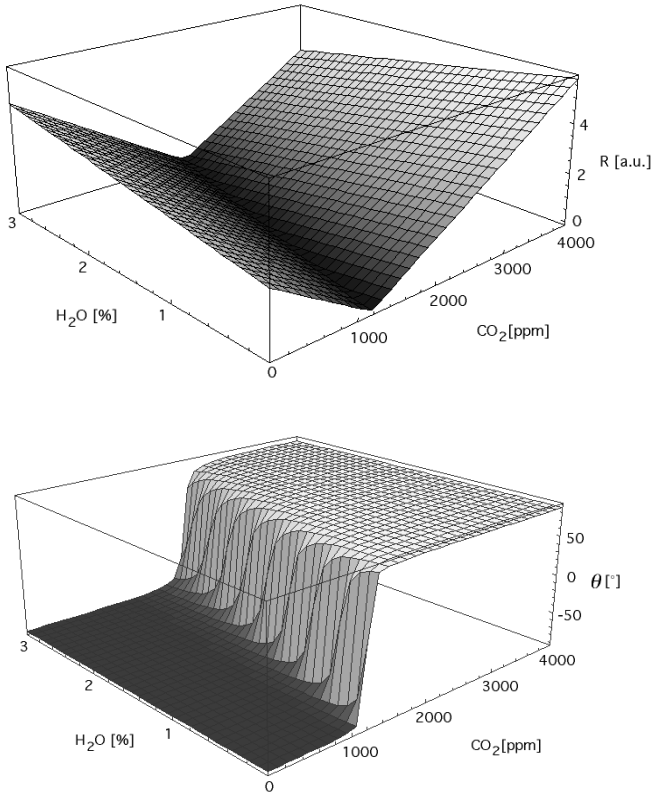

Fig. 1. Photoacoustic signal amplitude R and phase θ at the main ethene (C_2H_4) absorption line 10P(14) of the $^{12}C^{16}O_2$ laser of a gas sample containing 100 ppb ethene and variable CO_2 and H_2O concentrations at atmospheric pressure. Data calculated for a modulation frequency $f = \omega/2\pi = 2860$ Hz

2 The Levenberg–Marquardt algorithm

2.1 Introduction

The Levenberg–Marquardt algorithm is a standard method for determining the parameters of nonlinear functions in least-squares problems. A brief summary of its main principles is given in the following. It is to our knowledge for the first time that this algorithm is applied to determine gas concentrations from resonant photoacoustic measurements of multicomponent gas mixtures. This nonlinear approach takes also the quadratic dependence of the water vapor continuum absorption on its concentration into account [8]. An extensive discussion of the algorithm's features and guidance for its prac-

tical implementation into computer programs can be found in the literature [9, 10].

2.2 Mathematical principles

In a least-squares regression problem with nonlinear model functions $y_{ij} \equiv y_i(\boldsymbol{x}_j, \boldsymbol{a})$, $i = 1, \ldots, n$, $j = 1, \ldots, m$, of known parameters $\boldsymbol{x}_j$ and unknown parameters $\boldsymbol{a}$, the set of parameters $\boldsymbol{a} \equiv \{a_k\}$, $k = 1, \ldots, p$, should be determined which minimizes the merit function

$$\chi^2(\boldsymbol{a}) \equiv \sum_{i,j} \left(\frac{y_{ij}^{\text{meas}} - y_i(\boldsymbol{x}_j, \boldsymbol{a})}{\Delta_{ij}} \right)^2 . \tag{20}$$

Here y_{ij}^{meas} denotes the experimentally determined value at $\boldsymbol{x}_j$ and Δ_{ij} denotes its standard deviation. At a minimum of $\chi^2(\boldsymbol{a})$, the gradient of $\chi^2(\boldsymbol{a})$ is necessarily equal to zero. Close to a minimum of the merit function, $\chi^2(\boldsymbol{a})$ can be approximated by a quadratic form. It is

$$\chi^2(\boldsymbol{a}) \approx \gamma - \boldsymbol{d} \cdot \boldsymbol{a} + \frac{1}{2} \boldsymbol{a} D \boldsymbol{a} \tag{21}$$

with a suitable constant γ and a vector $\boldsymbol{d}$ of the dimension p. D indicates the Hessian matrix of $\chi^2(\boldsymbol{a})$ with the elements

$$D_{kl} \equiv \frac{\partial^2 \chi^2(\boldsymbol{a})}{\partial a_k \partial a_l} = 2 \sum_{\substack{i=1,\ldots,n \\ j=1,\ldots,m}} \frac{1}{\Delta_{ij}^2} \left[\frac{\partial y_i(\boldsymbol{x}_j, \boldsymbol{a})}{\partial a_k} \frac{\partial y_i(\boldsymbol{x}_j, \boldsymbol{a})}{\partial a_l} - \left[y_{ij}^{\text{meas}} - y_i(\boldsymbol{x}_j, \boldsymbol{a}) \right] \frac{\partial^2 y_i(\boldsymbol{x}_j, \boldsymbol{a})}{\partial a_k \partial a_l} \right] . \tag{22}$$

In order to simplify the calculations somewhat, the second derivatives in the last term of the above equation are neglected in the following [9].

From (21) the set of parameters $\boldsymbol{a} \equiv \{a_k\}$, $k = 1, \ldots, p$, which minimizes $\chi^2(\boldsymbol{a})$ can be calculated in a single step. It is given by

$$\boldsymbol{a}_{\min} = \boldsymbol{a}_{\text{current}} + \boldsymbol{D}^{-1} \left[-\nabla \chi^2(\boldsymbol{a}_{\text{current}}) \right] , \tag{23}$$

where the operator ∇ denotes the gradient.

If the merit function is not sufficiently well approximated by the quadratic form to determine $\boldsymbol{a}_{\min}$ by (23) a better set of parameters $\boldsymbol{a}$ can be derived iteratively by calculating

$$\boldsymbol{a}_{\text{next}} = \boldsymbol{a}_{\text{current}} - \text{const} \nabla \chi^2(\boldsymbol{a}_{\text{current}}) . \tag{24}$$

Thereby the constant in this equation must be sufficiently small in order not to exceed the minimum of the merit function. Hence, by approximating the minimum of $\chi^2(\boldsymbol{a})$ iteratively and then using (23), a good approximation to the best parameter set $\boldsymbol{a}_{\min}$ can be obtained.

2.3 Application of the algorithm to resonant PA measurements

The application of the Levenberg–Marquardt algorithm to PA measurements requires the calculation of $\chi^2(\boldsymbol{a})$ and its derivatives of the unknown parameters a_k. For photoacoustic measurements the model functions $y_i(\boldsymbol{x}_j, \boldsymbol{a})$ are given by (19) and (20) and the parameters to be determined are the concentrations of the individual components of a gas mixture. The index j represents the measurement at a specific laser line. The known parameters $\boldsymbol{x}_j$ are determined by the known absorption coefficients of the individual components and further known data such as the chopper frequency, the laser power, the air pressure, the molecular relaxation times presented in Table 1 and the energy ratio β.

With the definitions

$$\begin{aligned} x_0 &\equiv \beta \alpha_{\text{C}} c_{\text{C}} \frac{\tau_{\text{N}}}{1 + (\omega \tau_{\text{N}})^2} , & a_0 &\equiv A , \\ x_1 &\equiv x_0 \omega \tau_{\text{N}} - \frac{1}{\omega} (\alpha_{\text{H}} c_{\text{H}} + \alpha_{\text{C}} c_{\text{C}}) , & a_1 &\equiv \theta_0 , \\ x_{n+1} &\equiv \frac{1}{\omega} \alpha_n \ (n = 2, \ldots, m) , & a_{n+1} &\equiv c_n \ (n = 2, \ldots, m) , \end{aligned} \tag{25}$$

(18) and (19) can be rewritten as

$$R \equiv y_1(\boldsymbol{x}_j, \boldsymbol{a}) = a_0 \left[x_0^2 + \left(x_1 - \sum_{i=2}^{n+1} a_i x_i \right)^2 \right]^{1/2} \tag{26}$$

and

$$\theta \equiv y_2(\boldsymbol{x}_j, \boldsymbol{a}) = \arctan \left(\frac{x_1 - \sum_{i=2}^{n+1} a_i x_i}{-x_0} \right) + a_1 . \tag{27}$$

The derivates of the two model functions are given by the Jacobian matrix

$$\frac{\mathrm{d}\boldsymbol{y}}{\mathrm{d}\boldsymbol{a}} = \begin{pmatrix} \dfrac{\partial y_1}{\partial a_0} & \dfrac{\partial y_1}{\partial a_1} & \cdots & \dfrac{\partial y_1}{\partial a_k}\Big|_{k \geq 2} & \cdots \\ \dfrac{\partial y_2}{\partial a_0} & \dfrac{\partial y_2}{\partial a_1} & \cdots & \dfrac{\partial y_2}{\partial a_k}\Big|_{k \geq 2} & \cdots \end{pmatrix} \tag{28}$$

with

$$\begin{aligned} \frac{\partial y_1}{\partial a_0} &= \left[x_0^2 + \left(x_1 - \sum_{i=2}^{n+1} a_i x_i \right)^2 \right]^{1/2} , \\ \frac{\partial y_1}{\partial a_1} &= 0 , \\ \left. \frac{\partial y_1}{\partial a_k} \right|_{k \geq 2} &= \frac{-a_0 x_k \sum_{i=2}^{n+1} a_i x_i}{\left[x_0^2 + \left(x_1 + \sum_{i=2}^{n+1} a_i x_i \right)^2 \right]^{1/2}} \end{aligned} \tag{29}$$

and

$$\begin{aligned} \frac{\partial y_2}{\partial a_2} &= 0 , \\ \frac{\partial y_2}{\partial a_1} &= 1 , \\ \left. \frac{\partial y_2}{\partial a_k} \right|_{k \geq 2} &= \frac{x_k}{x_0} \left[1 + \left(\frac{x_1 - \sum_{i=2}^{n+1} a_i x_i}{-x_0} \right) \right]^{-1} . \end{aligned} \tag{30}$$

By introducing the above relations into (22) to (24), the merit function $\chi^2(\boldsymbol{a})$ can be minimized. The scaling factor A as well as the phase offset θ_0 and the gas concentrations of the individual components of the gas mixtures can then be determined with the Levenberg–Marquardt algorithm.

3 Experimental section

3.1 The mobile PA spectrometer

Our PA spectrometer has been designed for the monitoring of air pollutants at various measuring sites and is therefore installed in a mobile trailer. A commercially available line-tunable cw CO_2 laser provides radiation at approximately 80 wavelengths between 9 and 11 μm. The laser beam is intensity-modulated by means of a mechanical chopper at a frequency corresponding to the strongest acoustic resonance of the PA absorption cell at approximately 2860 Hz with a Q value of 168. The small resonance width of 17 Hz requires accurate control of the resonance frequency. The cell construction is based on the original design by Gerlach and Amer [11], extended by two buffer volumes to further reduce the noise induced by flowing gas when operated in the flow-through mode. It has a volume of 1.8 l and is usually operated at flow rates between 0.5 and 2 l/min. The acoustic signal generated by the absorption of the gas sample is recorded by two electret microphones and a lock-in amplifier. The signals are normalized with the laser power to account for power fluctuations in independent measurements. The system can be operated fully automaticly and exhibits detection limits in the ppb range for various compounds. A detailed technical description of the mobile spectrometer and of its calibration with gases of certified concentrations and known absorption cross sections reported by various authors, can be found elsewhere [4, 12].

3.2 Generation of multicomponent mixtures

Multicomponent mixtures containing water vapor and CO_2 at typical ambient concentrations have been generated in order to test the fit algorithm. The experimental set-up for the generation of these gas mixtures is plotted in Fig. 2. The commercial gas mixing unit (MKS, model 147C) consists of a computerized control unit and up to eight mass flow controllers that can be operated individually or in a master–slave mode. Two mass flow controllers with a full scale range of 2 l/min, three with 10 cm^3/min, one with 100 cm^3/min, one with 1 cm^3/min for the reference gas nitrogen and finally one with a full-scale range of 10 cm^3/min for pure CO_2 enabled us to dilute certified gases from bottles. These contained the individual compounds either in pure form or diluted in synthetic air at concentrations of 100 ppm. Due to its strong chemical reactivity, ozone was generated separately from pure synthetic air with a calibrated generator (Environics, model S100) and was consecutively added to the gas mixture. The actual concentrations were calculated from the mixing ratios of the gases and compared to the photoacoustically derived concentrations. Since water vapor and CO_2 concentrations can easily be monitored with commercial equipment, the concentrations of these two compounds were recorded in addition with a dew point mirror, a capacitive humidity meter and an infrared absorption monitor for CO_2 (LI-COR, model LI-6262). The latter device operated at the strong CO_2 absorption band at 4.26 μm and provided a detection limit of a few ppm CO_2.

4 Results and discussion

First we present two examples from a number of artificially generated multicomponent gas mixtures with time-varying concentration profiles, followed by examples of an analysis of sampled air and a field study.

4.1 Three-component mixture containing ethene (C_2H_4), *water vapor and* CO_2

Figure 3 presents the analysis of a three-component mixture with ethene, water vapor and CO_2. The concentration of CO_2 was increased stepwise from 0 ppm up to a final concentration of 4000 ppm while the absolute humidity and the ethene concentrations were kept at constant levels of 1.3% and 100 ppb, respectively. Figure 3 shows the variation of the photoacoustic signal amplitude and phase with time at three laser transitions. The 10P(14) transition is characteristic for ethene absorption and the 10R(20) transition for water vapor line absorption, while none of them show appreciable absorption at the 10P(12) transition. With increasing CO_2 concentration the signal amplitudes at the 10P(14) and the 10R(20)

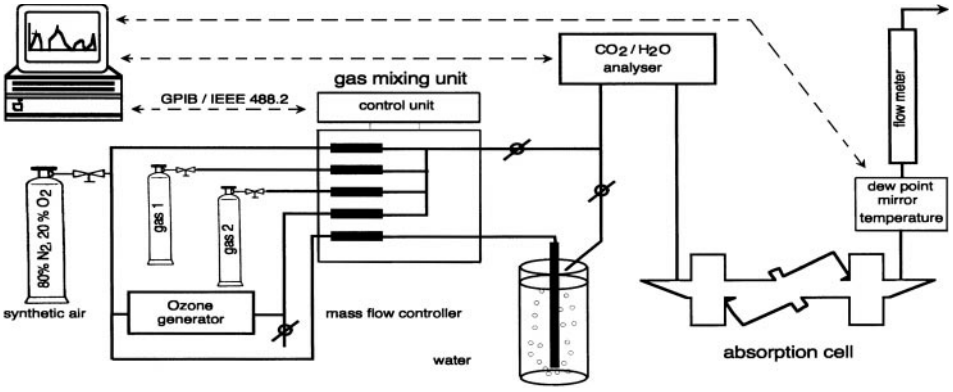

Fig. 2. Experimental set-up for the generation of calibrated gas mixtures. Certified gases from bottles containing pure compounds or single compounds diluted in synthetic air at a concentration of typically 100 ppm have been mixed with mass flow controllers. Ozone was generated separately during the measurements with a calibrated ozone generator (Environics, model S100) as well as water vapor that was generated by flowing synthetic air with a separate mass flow controller through a gas washing bottle with pure water. Ozone and water vapor were both mixed with the other gases at the gas inlet of the absorption cell

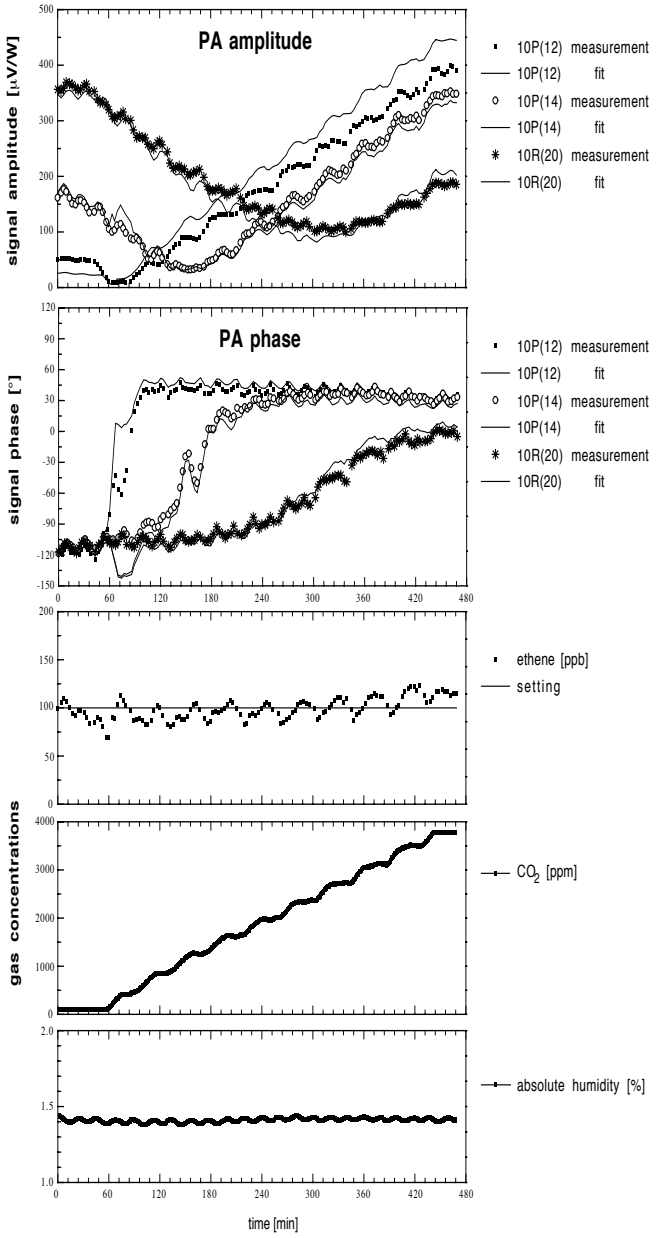

Fig. 3. Example of the analysis of a gas mixture containing water vapor, ethene and a varying CO_2 concentration in synthetic air. In the two upper plots measured (*dots*) and theoretically calculated (*lines*) photoacoustic amplitude and phase with respect to the modulated exciting laser radiation are shown for three CO_2 laser lines. The 10R(20) and 10P(14) laser transitions represent water vapor and ethene absorption, respectively, while the 10P(12) transition is unspecific. The photoacoustic amplitude and phase depend strongly on the amount of water vapor and of CO_2 present in the gas sample. The ethene concentration could be derived from the above data with the Levenberg–Marquardt algorithm. Good agreement is obtained with the expected value of 100 ppb

transitions decrease due to destructive signal interferences of the ethene and water vapor absorption with the absorption of CO_2. The amplitudes increase again when the CO_2 absorption becomes dominant. As Fig. 3 implies, the signal phases at the three lines start at the same experimental value of $-110°$ and consecutively increase up to a final value of 50° when CO_2 absorption becomes dominant. The measured signal amplitude and phase at the 10P(14) transition can qualitatively be compared with the calculated data in Fig. 1. In analogy to the case of Fig. 1, the minimum signal amplitude is passed at CO_2 concentrations slightly above 1000 ppm simultaneously with a rapid increase of the signal phase. The measured amplitudes and phases are well approached by the Levenberg–Marquardt algorithm. In addition to the plotted data measurements at the 10P(16) and the 10P(20) laser lines have been performed. In agreement with the Levenberg–Marquardt fit, these show a similar time dependence as the depicted data. They have, however, been omitted for clarity in Fig. 3. The resulting ethene concentration was derived by fitting the signal amplitude and phase at all five laser lines with equal weights. As the bottom part of Fig. 3 shows, the ethene concentration remains at the expected value of 100 ppb according to the setting of the gas mixing unit with slow variations on the order of 25 ppb. Variations can also be observed in the concentrations of the other two compounds. They are caused by thermal drifts of the mass flow controller zero points due to temperature fluctuations during the measurement. The CO_2 and H_2O concentrations depicted in Fig. 3 have been obtained from the LI-COR infrared absorption monitor and the dew point mirror, respectively. The data were used to determine intial estimates for the fitting procedure.

4.2 Four-component mixture containing ethene (C_2H_4), *methanol* (CH_3OH), *water vapor and* CO_2

At a constant absolute humidity of approximately 1.6%, the CO_2 concentration was increased stepwise from 0 ppm up to 2250 ppm. Up to this point the ethene concentration was kept constant at 50 ppb and then increased in a single step to 200 ppb. As a fourth component, methanol was added to the mixture. Like ethene, methanol is an important compound in industrial emissions and also frequently encountered in biological systems. The methanol concentration was always kept constant at 100 ppb. After a final increase to a maximum CO_2 concentration of 2500 ppm the CO_2 concentration was reduced in steps of approximately 240 ppm until no CO_2 was present in the gas mixture. The slight asymmetry of the CO_2 concentration profile observed in Fig. 4 was caused by an erroneous setting of the gas mixing unit. It did not, however, affect the measurements themselves. As is clear from Fig. 4, the photoacoustic amplitudes and phases show the expected variations with time and the ethene and methanol concentrations derived from these data agree well with the expected values according to the settings of the gas mixing unit.

4.3 Air sample from a fruit storage chamber

Besides the analysis of artificial gas mixtures, the algorithm has been applied to PA spectra of an air sample from an apple storage chamber. Plants and fruit emit various gases that give evidence of biological processes [13–18]. Ethene, for example, reacts as a ripening and stress hormone. It is produced in large quantities by apples and can be excellently monitored with the $^{12}C^{16}O_2$ laser. At the Swiss Federal Research Station for Fruit-Growing, Viticulture and Horticulture in Wädenswil/Zurich different fruit are exposed to artificially modified atmospheric conditions. These experiments are aimed at elucidating the biological processes entailed with the ripening of fruit. An air sample of 5 l volume and unknown composition was collected with a gas sampling bag

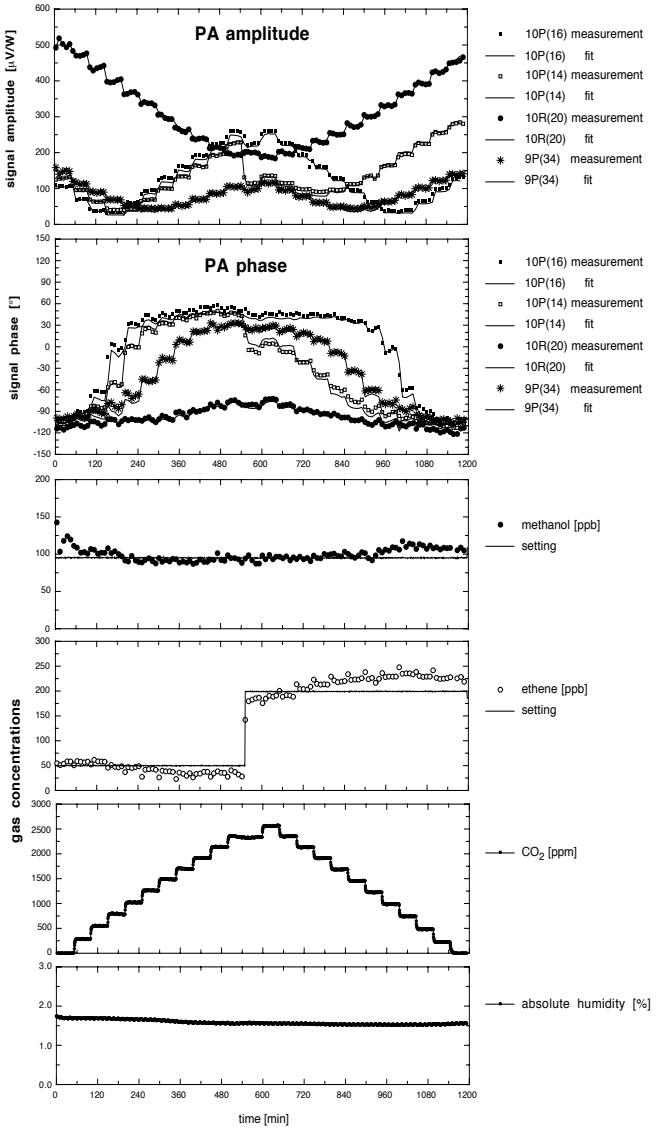

Fig. 4. Analysis of a multicomponent mixture containing ethene, methanol, water vapor and CO_2. Again, the calculated signal amplitudes and phases are in excellent agreement with the measured data and the derived methanol and ethene concentrations correspond to the expected levels

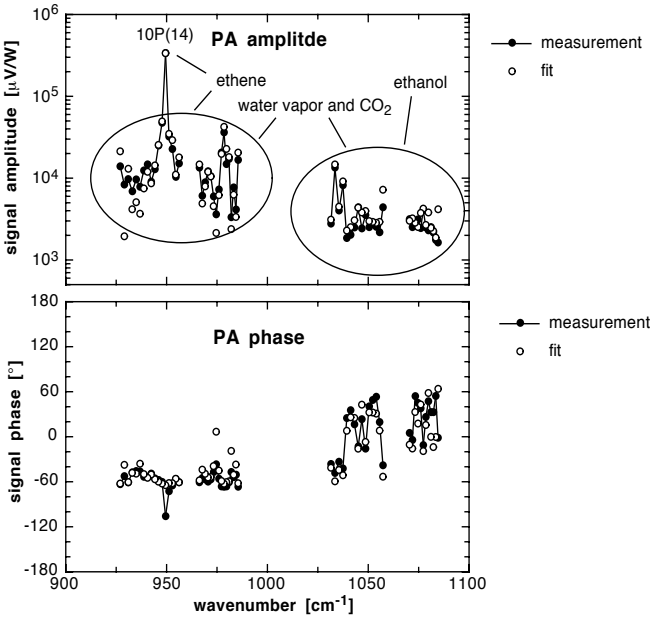

Fig. 5. Photoacoustic absorption spectrum of an air sample from a fruit storage chamber. The measured photoacoustic amplitude and phase and the data obtained with the Levenberg–Marquardt algorithm are plotted. The corresponding gas concentrations resulting from the fit are given in Table 2

(Linde plastigas) from an apple storage chamber with enhanced CO_2 concentration. The consecutive analysis was performed within 24 h in a sealed-off measurement with our PA system at ambient pressure and at room temperature. The result is displayed in Fig. 5. The spectra are dominated by the absorption of ethene. Furthermore, evidence for ethanol can be found at the 9P laser lines. This alcohol can most probably be ascribed to anaerobic breath processes of the fruit. Four full $^{12}C^{16}O_2$ laser absorption spectra have been recorded and almost no deviation between the spectra was observed.

Figure 5 shows one PA amplitude and phase spectrum as well as the corresponding data calculated with the Levenberg–Marquardt fit. Reference spectra of ethene, ethanol, water vapor and of CO_2 have been included into the fit procedure. Except for a few laser lines in the 10P branch, the measured photoacoustic amplitude and phase could be reproduced accurately. The correspondence between fitted and measured amplitude and phase spectra gives evidence to the supposition that besides water vapor, CO_2, ethene and ethanol only few, if any, further absorbing compounds were present in the air sample. The gas concentrations derived with the Levenberg–Marquardt fit procedure are listed in Table 2. They represent average concentrations obtained from the analysis of all four spectra. Due to the large overlap in the absorption regions in the 9P laser branch the inclusion of further compounds, such as methanol, into the fit resulted in a larger deviation of the fitted from the measured spectra and consequently in erroneous gas concentrations. The derived ethene concentration of 220 ppm and the ethanol concentration of 22.3 ppm are rather high compared to concentrations usually found in ambient air. They correspond, however, to the expected levels in the fruit storage room according to earlier air analyses and independent studies at other locations [19, 20].

4.4 Ambient air monitoring at Alptal (Switzerland)

The field study was performed at Alptal (Switzerland), approximately 40 km to the south of Zurich, where a biological monitoring station is operated by the Swiss Federal

Table 2. Gas concentrations in an air sample from an apple storage room. The errors quoted are the standard deviations of the concentrations derived from four fitted spectra

Gas	Concentration
Ethene (C_2H_4)	220 ± 14 ppm
Ethanol (C_2H_6O)	22.3 ± 0.5 ppm
Carbon dioxide (CO_2)	$2.80 \pm 0.3\%$
Water vapor (H_2O)	$0.73 \pm 0.01\%$

Institute for Forest, Snow and Landscape Research (WSL Birmensdorf/Zurich) in a mountain valley far from primary air pollution sources. Between July 5 and July 24, 1996, the mobile PA system was operated at the unattended meteorological monitoring site "Erlenhöhe" at an altitude of 1200 m above sea level. The monitoring site is situated on a slightly descending slope in a lightly wooded area. Neither agricultural activities nor any traffic were present in the immediate environment. Harsh meteorological conditions during the measurement period and large diurnal temperature variations with maximum temperatures exceeding 35 °C and minimum temperatures close to 7 °C posed a challenge to the performance of the automatic system, particularly in view of the fact that the air conditioning in the trailer had to be switched off due to the low electrical power available at that site. Thermal expansion of the laser resonator caused by the temperature variations resulted in the detuning of some of the laser transitions. Particularly in the 9R laser branch single lines needed to be realigned several times during the course of the campaign. Hence, some critical laser transitions have been excluded in the evaluation of the spectra. Despite these minor difficulties, however, the overall performance of the system was good during the monitoring period and complete $^{12}C^{16}O_2$ laser absorption spectra could be recorded during the 20 days. The system was operated in the flow-through mode, i.e. ambient air was continuously drawn into the absorption cell through a 5-m-long teflon PFA tube at a flow rate of approximately 1 l/min.

The PA spectra (amplitude and phase) recorded during the field study at Alptal gave clear evidence of (a) ozone with characteristic signals of the main ozone absorption band at $^{12}C^{16}O_2$ laser wavelengths (9P(14) laser line) and (b) water vapor and CO_2. To check for further trace components at the measuring site, two air samples were drawn on a hot summer day after a six-day period of stable meteorological conditions with bright weather and without rainfall. The samples were analysed at the Paul Scherrer Institute (PSI) at Würenlingen (Switzerland), with a gas chromatography system, and revealed low ambient concentrations of isoprene (2 ppb), of ethene and ethine (0.4 ppb) and of further hydrocarbons. Except for isoprene all concentrations were below 1 ppb and thus substantially lower than the detection limit of our mobile PA system. The ambient hydrocarbon concentrations were also lower than those of a comprehensive study on volatile organic compounds at rural sites in Europe [21]. Another strongly absorbing compound at CO_2 laser wavelengths was ammonia (NH_3). However, an earlier study with denuder measurements at a nearby site revealed yearly average NH_3 concentrations of only $0.20 \pm 0.17\,\mu g/m^3$ (≈ 0.3 ppb) [22], which is also below the detection limit of 2 ppb of our mobile system. Thus, since no evidence could be found for absorbing compounds other than ozone, water vapor and CO_2 at relevant concentration levels, we analyzed the recorded PA spectra by taking into account calibration spectra of these three species only. Best results were obtained by restricting the Levenberg–Marquardt fitting procedure to the 9P laser branch that exhibits the strongest ozone absorption at $^{12}C^{16}O_2$ laser frequencies. Additionally the 10R(18), 10R(20) and 10R(22), as well as the 10P(18), 10P(20) and 10P(22) transitions have been included since they are representative for H_2O and CO_2 absorption. Both signal amplitude and phase were fitted with the same statistical weight.

Figure 6 depicts the concentration profiles of the three gases at the measuring site between July 5 and July 24, 1996. In comparison to the photoacoustic measurements, the ozone concentrations derived with the commercial ozone analyser of the WSL Birmensdorf and the absolute humidity calculated from the data of a capacitive humidity meter are plotted. The CO_2 concentrations in Fig. 6 have been obtained from the near-infrared gas sensor (Gas Card) of the mobile system. The photoacoustic ozone concentrations show the expected variations in the daytime in correlation to the data obtained with the commercial monitor. Average concentrations are on the order of 40 ppb during the measuring period while maximum

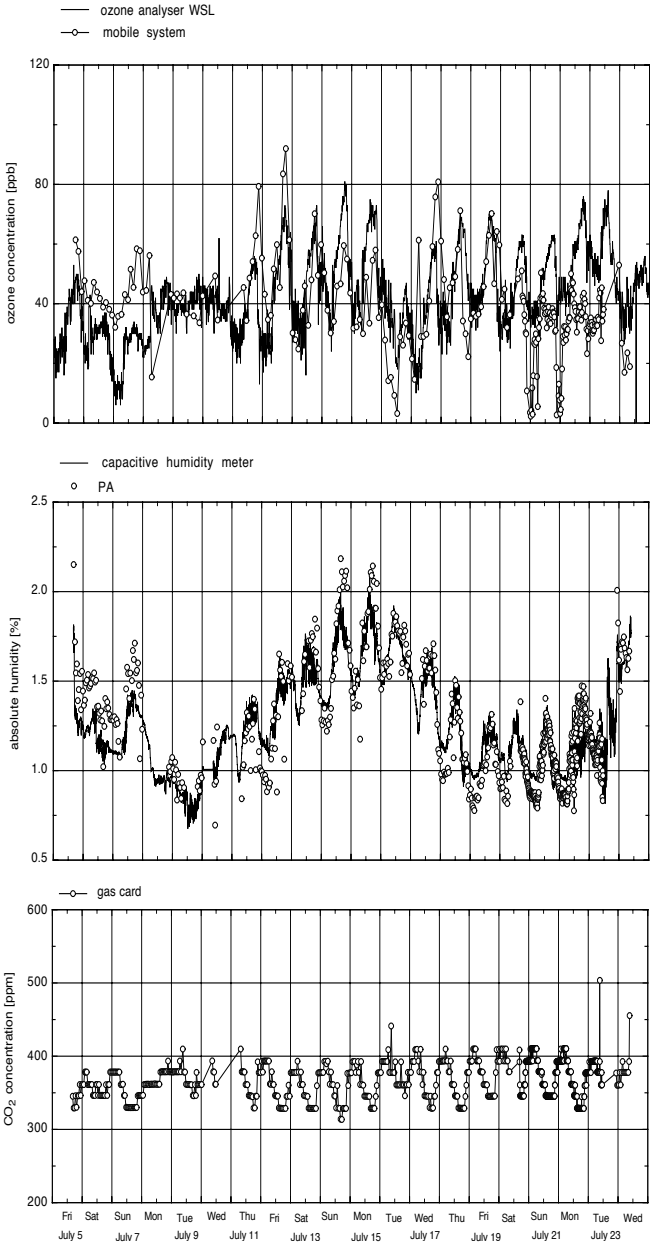

Fig. 6. Ozone, water vapor and CO_2 concentrations at the meteorological monitoring site Erlenhöhe (Brunni, Switzerland) between July 5 and July 24, 1996. The concentration profiles derived from the photoacoustic spectra of ozone and of the absolute humidity are compared with the data from a commercial ozone analyser of the Swiss Federal Institute for Forest, Snow and Landscape Research (WSL Birmensdorf) and with the absolute humidity calculated from the data of a capacitive humidity meter

concentrations reach up to approximately 80 ppb. In contrast to the data from the commercial monitor the photoacoustic concentrations come close to zero on July 16. This could most probably be ascribed to erroneous results of the fitting procedure when the ozone concentrations come close to our detection limit of 13 ppb. The natural background concentration of ozone in clean tropospheric air exceeds 20 $\mu g/m^3$, i.e. 10 ppb [23]. The ambient ozone concentration is increased above this level by ozone originating from local precursors at distances between 10 and 50 km and by contributions from higher atmospheric layers where ozone concentrations remain at rather constant levels even in periods of bad weather. Ambient ozone concentrations below 10 ppb are therefore not very probable. The mismatch between the concentrations determined photoacoustically and the data from the commercial system between July 22 and July 24 can be ascribed to thermal detuning of laser transitions in the 9P laser branch. This resulted in larger measurement errors of the recorded spectra. It is very unlikely that such deviations are caused by ozone reactions in the gas tubings because similar tube lengths have been used for the calibration measurements and the field studies and, furthermore, the deviations occur in both directions.

The absolute humidity determined from the photoacoustic data is in good agreement with the conventionally measured concentration. It shows diurnal variations with amplitudes on the order of 0.75% and an additional slow modulation with time caused by the changing meteorological conditions. The CO_2 concentrations exhibit diurnal variations around 350 ppm with maximum values after midnight on the order of 400 ppm and minimum concentrations around 330 ppm in the afternoons. No comparative data were available for the CO_2 measurements depicted in Fig. 6. However, the CO_2 data were used to derive the ozone concentrations from the photoacoustic spectra. The good agreement between the measured and the calculated photoacoustic spectra sustain the assumption that the correct CO_2 concentrations were determined with the near infrared gas analyser. Diurnal and seasonal changes in atmospheric CO_2 concentrations in different environments have recently been investigated by various authors [24–26]. In these studies, diurnal variations of the CO_2 concentration with enhanced concentrations during nighttime, minimum concentrations in the afternoon and differences between maximum and minimum concentrations on a single day in summer of 50 up to 95 ppm were observed. The enormous diurnal variation of CO_2 is ascribed to the daily cycle of photosynthesis and respiration by the surrounding vegetation superimposed on the day–night contrast of atmospheric mixing [25]. These results agree well with our CO_2 measurements. It should be noted that the diurnal CO_2 variation is less pronounced during the first six days of the monitoring period, which were characterized by rather bad weather with low solar radiation densities and hence reduced photosynthesis activity. Our CO_2 data are also supported by a previous study performed in a rural area with enhanced CO_2 concentrations during night time [1, 4].

5 Conclusion

On the basis of the numerical method of Levenberg–Marquardt we developed a new fitting algorithm for the analysis of photoacoustic spectra of multicomponent gas samples taken with a line-tunable CO_2 laser. In contrast to previous analyses this algorithm calculates signal amplitudes and phases separately, which extends the potential of the analysis substantially, particularly with respect to multicomponent mixtures which often cause interfering spectra. Without any pre-treatment air samples of different origin can thus be analyzed.

With a commercial gas mixing device the analysis procedure was tested for the first time with multicomponent mixtures containing time-varying gas concentrations. The mixtures were prepared with water vapor and CO_2 at ambient concentrations and additional compounds in the ppb range. Excellent agreement between measured photoacoustic amplitude and phase spectra and the data calculated from reference spectra of the individual compounds was obtained. The derived gas concentrations are in good agreement with the expected values according to the settings of the gas mixing unit. Deviations are on the order of 10% to 20%. Furthermore, the algorithm was applied to the analysis of an air sample of unknown composition from an apple storage chamber. Except for a few laser lines, excellent agreement between the measured and the calculated data was obtained by including reference spectra of water vapor, CO_2, ethene and ethanol vapor into the fitting procedure. The resulting gas concentrations correspond to the expected levels according to earlier investigations.

In a field campaign our mobile CO_2 laser photoacoustic system was operated unattended at a biological monitoring site in a rural mountainous area at an elevation of 1200 m above sea level. The ambient air was flown continuously through the gas cell. Photoacoustic spectra were recorded over 20 days and analyzed after the campaign. Water vapor, CO_2 and ozone could easily be identified from the spectra and their diurnal variations were derived, but no evidence was found for additional absorbing compounds. Independent analyses of air samples showed that the concentrations of volatile organic compounds were in fact below the detection limit of our system. In contrast to laboratory measurements on gas mixtures containing only known compounds, field measurements have larger errors in derived trace concentrations in ambient air due to potential absorption interferences of unknown species.

With regard to future field measurements at sites with low ambient pollutant concentrations, emphasis is thus put on lowering these detection limits, e.g., by implementing a multipass photoacoustic cell. On the other hand, an improvement in detection selectivity, which is particularly important in highly polluted areas, is envisaged by increasing the number of operational wavelengths, e.g., by the simultaneous operation of two different laser isotopes. Ideally, a narrow-band continuously tunable laser with a broad wavelength range in the mid-IR is employed and great efforts are currently being put into the development of such sources that are suitable also for field measurements.

Acknowledgements. We are grateful to the help provided by the Swiss Federal Research Station for Fruit-Growing, Viticulture and Horticulture in Wädenswil/Zurich and for the support and the comparative ozone data obtained from the Swiss Federal Institute for Forest, Snow and Landscape Research (WSL Birmensdorf/Zurich). We owe special thanks to Victor Stadelmann (PSI Würenlingen) for the gas chromatography analysis of two air samples. This project is supported by the Swiss National Science Foundation and the ETH Zurich.

References

1. M.W. Sigrist (Ed.): *Air Monitoring by Spectroscopic Techniques*, Chem. Analysis, Vol. 127, Chap. 4 (Wiley, New York 1994)
2. A.D. Wood, M. Camac, E.T. Gerry: Appl. Opt. **10**, 1877 (1971)
3. P.L. Meyer, M.W. Sigrist: Rev. Sci. Instrum. **61**, 1779 (1990)
4. A. Thöny, M.W. Sigrist: Infrared Phys. Technol. **36**, 585 (1995)
5. R.A. Rooth, A.J.L. Verhage, L.W. Wouters: Appl. Opt. **29**, 3643 (1990)
6. V.P. Zharov, V.S. Letokhov: *Laser Optoacoustic Spectroscopy*, Springer Series in Optical Sciences, Vol. 37 (Springer, Berlin, Heidelberg 1986)
7. E. Fermi: Z. Phys. **71**, 250 (1931)
8. J. Hinderling, M.W. Sigrist, F.K. Kneubühl: Infrared Phys. **27**, 63 (1987)
9. W.H. Press, B.P. Flannery, S.A. Teukolsky, W.T. Vetterling: *Numerical Recipes in Pascal. The Art of Scientific Computing* (Cambridge University Press, Cambridge 1989)
10. H.R. Schwarz: *Numerische Mathematik* (B.G. Teubner, Stuttgart 1988)
11. R. Gerlach, N.M. Amer: Appl. Phys. **23**, 319 (1980)
12. M.A. Moeckli: PhD Thesis, No. 12150, Swiss Federal Institute of Technology (ETH) Zurich, Switzerland (1997)
13. H. Mehlhorn, A.R. Wellburn: Nature **327**, 417 (1987)
14. D.M. Reid: *Ethylene – a possible factor in the response of plants to air pollution and acid precipitation*, In: NATO ASI Series, G16 (Springer, Berlin 1987) pp. 241–254
15. H. Mehlhorn, B.J. Francis, A.R. Wellburn: New Phytol. **110**, 525 (1988)
16. Y.M. Chen, A.R. Wellburn: Plant Physiol. **91**, 357 (1989)
17. F.B. Abeles, P.W. Morgan, M.E.Jr. Salveit: *Ethylene in Plant Biology*, 2nd edn. (Academic Press, New York 1992)
18. H.S.M. De Vries, M.R. Van Lieshout, F.J.M. Harren, J. Reuss: Infrared Phys. Technol. **36**, 483 (1995)
19. E. Höhn: Swiss Federal Research Station for Fruit-Growing, Viticulture and Horticulture, Wädenswil/Zurich, private communication (1997)
20. P. Perlmutter, S. Shtrikman, M. Slatkine: Appl. Opt. **18**, 2267 (1979)
21. S. Solberg, C. Dye, N. Schmidbauer, A. Herzog, R. Gehrig: J. Atmos. Chem. **25**, 33 (1996)
22. A. Fischer-Riedmann: PhD Thesis, No. 11035, Swiss Federal Institute of Technology (ETH) Zurich (1995)
23. Bundesamt für Umwelt, Wald und Landschaft (BUWAL): Schriftenreihe Umwelt Nr. 277, Report, Bern (1996)
24. M. Veste, W.B. Herppich: Photosynthetica **31**, 371 (1995)
25. P.T. Tans, P.S. Bakwin, D.W. Guenther: Global Change Biol. **2**, 309 (1996)
26. D. Fowler, K.J. Hargreaves, J.A. Macdonald, B. Gardiner: Forestry **68**, 327 (1995)